Axis switching in low to moderate aspect ratio rectangular orifice synthetic jets

Joseph C. Straccia and John A. N. Farnsworth*
Ann and H.J. Smead Department of Aerospace Engineering Sciences, University of Colorado Boulder, Boulder, Colorado 80309, USA

(Received 19 October 2020; accepted 21 April 2021; published 12 May 2021)

The dynamics of finite-span vortex rings expelled from a synthetic jet actuator is studied experimentally using stereoscopic particle image velocimetry as well as being modeled with an inviscid Biot-Savart velocity induction solver. Five rectangular orifices are tested with aspect ratios AR of 2, 4, 6, 13, and 19 at a single actuator stroke length. In the lower synthetic jet, vortex ring axis switching is the dominant factor influencing the jet's shape, while in the upper jet, viscous diffusion plays a more critical role. The variations in the jet's width driven by vortex ring axis switching becomes more extreme with increasing orifice AR. The height of the first axis switch also increases with AR, and for the three lowest AR values tested, the jet axis switches two to three times. However, at orifice AR of 13 and 19, the jet only axis switches once. The lack of additional axis switching is shown to be due to a collision of the vortex ring with itself after the first axis switch and a subsequent bifurcation of the vortex ring. The critical AR limit above which vortex ring bifurcation occurs is found to be consistent with prior work on isolated vortex rings. The axial profiles of centerline velocity for the AR = 4–19 jets exhibited two local peaks which become more prominent with increasing jet AR. These variations in centerline velocity are also predicted by the inviscid solver, indicating that they are most likely due to the dynamics of the primary vortex ring and not secondary structures as previously hypothesized.

DOI: 10.1103/PhysRevFluids.6.054702

I. INTRODUCTION

Synthetic jet actuators (SJAs) are a type of active flow control device that can add momentum to a flow field without a net addition of mass. They are able to achieve this feat because an oscillating driver, such as a piston, voice coil, or piezoelectric disk, periodically draws external fluid into the actuator cavity and then expels that same fluid back out of the orifice. The periodic ejection of fluid from the orifice is an efficient excitation mechanism for rapid vortex ring formation when compared to the generation of coherent structures in continuous jets due to either instability or forcing [1,2]. As a consequence, the entrainment rate in the lower region of synthetic jets is superior to that of continuous jets [3–5]. The vortex rings are also critical in enabling the formation of the synthetic jet and in transporting momentum through the external flow field [6,7].

The potential applications of synthetic jets are many and varied, including controlling external and internal flow separation [8,9], providing flight control for maneuvering aircraft [10], enhancing heat transfer via jet impingement [11], vectoring steady jets [12], and increasing mixing in reacting flows [13]. In many of these applications jet entrainment and mixing are important attributes influencing the effectiveness of the flow control. For example, in thrust vectoring high entrainment in the synthetic jet is crucial in establishing the pressure gradient which provides the lateral force to

*john.farnsworth@colorado.edu

turn the coflowing steady jet [14]. In separation control the jet's ability to entrain high momentum free stream fluid down into an adverse pressure gradient boundary layer can help mitigate flow separation [15]. In reacting flows the vortex dynamics of nonaxisymmetric jets can provide not only large-scale mixing, brought about by self-induced deformations, but also critical small-scale turbulent mixing which is enhanced by the vortex ring azimuthal instability modes [16].

When a SJA utilizes a nonaxisymmetric orifice the shape of the resulting jet fluctuates as it flows downstream due to self-induced deformations of the vortex rings. For noncircular vortex rings with symmetric shapes, these deformations give rise to a phenomenon called axis switching, whereby the vortex ring major axis contracts and the minor axis expands until the original minor axis becomes the new major axis and vice versa. The lateral deformations of the vortex rings during this process cause external fluid to be engulfed into the jet, thereby increasing the jet's entrainment [17,18]. Therefore, a clear understanding of vortex dynamics in synthetic jets is essential for any study seeking to maximize the performance of synthetic jets in flow control applications.

Axis switching has been studied for decades in isolated vortex rings, with the earliest work employing inviscid models that closely matched physical observation [19–23]. The inviscid approximation is reasonable in the regions of an irrotational fluid around a vortex where the induced velocity depends more on the circulation strength of the vortex than on the distribution of vorticity within the core. Therefore, the diffusion of vorticity in the core can be ignored and the vortex approximated as a line vortex with either an irrotational vortex profile or a Rankine vortex profile with a fixed core size [19–21]. Of course, inviscid techniques cannot model vortex formation, decay, or collisions, as they are inherently viscous processes.

The governing equation for the inviscid incompressible propagation of an ideal vortex ring is the Biot-Savart law. A differential form of the Biot-Savart law is

$$d\mathbf{V} = \frac{\Gamma}{4\pi}\frac{\mathbf{dl}\times\mathbf{r}}{|\mathbf{r}|^3}, \tag{1}$$

where V is the induced velocity at point P, Γ is circulation, dl is a discreet segment of the line vortex, and r is the vector between P and the line segment dl.

It can be shown that the local self-induced velocity of a curved irrotational vortex is proportional to the curvature of the vortex axis and that all noncircular vortex rings therefore "wobble" as they propagate [19]. Consider, for example, a bisymmetric elongated vortex ring with curved ends and a rectilinear midsection (see the t_0 vortex ring in Fig. 1). This is a reasonable approximation for the shape of a vortex ring that would form from an elongated rectangular orifice or nozzle. Initially, the ends of the vortex ring, possessing high curvature, travel downstream faster than the middle. This gives the ring the appearance that it is folding along its minor axis (see t_1 and t_2 in Fig. 1). Before the vortex ring actually folds in half, however, the previously low curvature middle region develops a bend and accelerates to catch up with the leading part of the ring (see t_2 and t_3 in Fig. 1). When the ring flattens back out, what was previously the major axis of the ring has become the minor axis, i.e., the vortex ring has axis switched (see t_4 in Fig. 1). From here the process can repeat, eventually returning the ring to its original orientation [20]. Various prior studies have found good agreement between the dynamics predicted by inviscid simulations of noncircular vortex rings and the observations made in experimental images and movies [20,21].

The many numerical and experimental studies investigating isolated vortex rings with elongated shapes (e.g., elliptic) have established a number of common findings about axis switching. For one, the aspect ratio AR of the vortex ring (i.e., the ratio of initial length to width) is the most important characteristic influencing the axis-switching behavior. In low AR vortex rings, which deviate only slightly from a circular shape, the deformations associated with axis switching are generally sinusoidal and relatively subtle. At higher AR these motions become more complex and the oscillations in the ring's width and length become larger [19,21–23]. The oscillation period and spatial wavelength of the axis-switching deformations also increases with AR, i.e., high AR vortex rings take a longer time and a greater distance to complete an axis switch than low AR rings do [21,23–25]. The half period of the oscillatory deformations is marked by the vortex ring's return

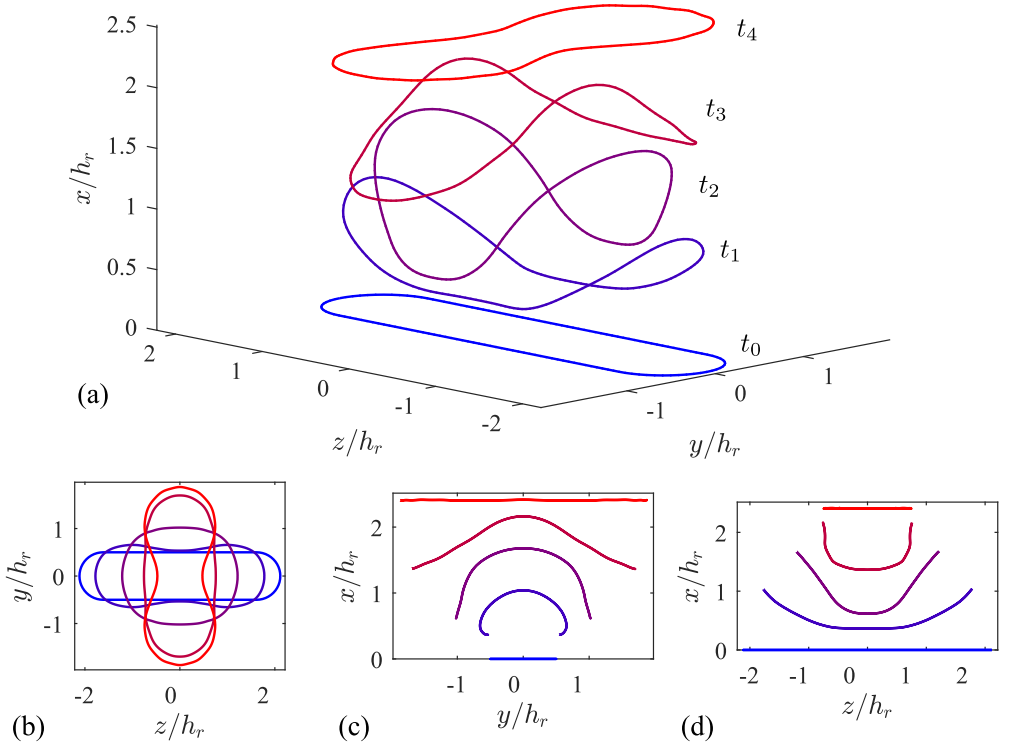

FIG. 1. Biot-Savart solver simulation of an $AR_r = 4.2$ vortex ring undergoing self-induced axis-switching deformations with the ring axis displayed at five instances, labeled t_0–t_4, and colored with increasing time from blue to red.

to a roughly planar configuration with the axes now reversed. The term "roughly planar" is used because the ring is typically not perfectly flat when the axis switch is completed (note that, although it is hard to tell due to the scale of the figure, the vortex ring at t_4 in Fig. 1 is not completely flat) [19–21], nor is the original shape of the vortex ring precisely recovered [19–21,25]. In particular, the vortex rings tend to develop a pinch in the middle of the long axis upon completion of the axis switch which, for certain conditions, can cause the antiparallel sides of the vortex ring to collide, leading to vorticity reconnection (see the shape of the t_4 vortex ring in Fig. 1) [21–23,25].

The axis-switching deformations continue as long as the vortex ring remains coherent and maintains its topology. However, the axial distance and time between axis switches increase with the number of switches [23,24]. This phenomenon has been attributed to the decline in circulation strength with time [23], although the growth of the vortex core size due to diffusion of vorticity is likely a contributing factor. It has been established that vortex rings with larger cores experience weaker local self-induction and are therefore slower to switch axes than thin core vortices [23,25,26]. The geometric oscillations of the vortex ring also change with time. Axis-switching deformations in noncircular vortex rings are due to an instability associated with the vortex geometry. With time, the oscillations slowly damp out as the vortex ring converges to a more stable circularized shape [20]. However, a fully circular vortex ring is unlikely to be achieved because viscous processes tend to limit the longevity of isolated noncircular vortex rings to only a few axis switches.

Axis switching of vortex rings is also well established in continuous jets [1,17,26]. The impact the AR has on the frequency of axis switching and the magnitude of the deformations for isolated

rings also apply to the vortex rings in continuous jets. However, in jets the self-induced deformations of the vortex ring also change the shape of the jet and, importantly, enhance the jet's entrainment rate [17]. This enhancement in entrainment and mixing have led some to propose nonaxisymmetric orifices as a mechanically simpler alternative to active techniques meant to achieve the same effect.

In general, less attention has been given to studying vortex ring axis switching in synthetic jets than in isolated vortex rings and continuous jets. The particle image velocimetry (PIV) measurements presented by Amitay and Cannelle [27] in AR = 50.8, 76.2, and 101.6 rectangular orifice synthetic jets reveal the typical variations in jet width associated with vortex ring axis switching, although the phenomenon was not explicitly identified in the discussion. The presence of these deformations in such large AR synthetic jets suggests that the phenomenon occurs over a very large range of vortex ring AR values. Van Buren *et al.* [28] were able to reconstruct the core axes of vortex rings produced by an AR = 12 synthetic jet revealing dynamics which qualitatively look very similar to those in isolated vortex rings. However, the AR = 6, 12, and 18 orifice synthetic jets tested switched axes only once. Straccia and Farnsworth [29] later showed that the lack of additional axis switching was due to bifurcation of the vortex rings. Lindstrom and Amitay [30] investigated synthetic jets with AR = 19 rectangular, trapezoidal, and triangular orifices and reported that all of the jets axis switched, albeit only once. Wang *et al.* [18] focused their experimental study on synthetic jets with lower AR rectangular orifices ranging from 1 to 5. While up to three vortex ring axis switches were measured in the AR = 2–4 orifice jets, the vortex ring from the AR = 5 orifice axis switched only once before bifurcating. When they compared their results to prior data from continuous jets, Wang *et al.* [18] found that the vortex rings in synthetic jets axis switch closer to the orifice. They attributed this difference to a slower convective speed in the synthetic jet, although the earlier formation of the vortex ring in the synthetic jet was probably also a contributing factor. As with continuous jets, Wang *et al.* [18] reported that axis switching in the nonaxisymmetric synthetic jets yielded a higher entrainment rate than that of a axisymmetric synthetic jet.

Unsurprisingly, Wang and Feng [31] found that noncircular vortex rings in a crossflow, which were produced by a rectangular orifice synthetic jet embedded in a flat plate, also axis switch. Furthermore, axis switching was observed whether the long axis of the orifice was aligned with the flow or perpendicular to it; however, the influence the orifice orientation had on the jet-crossflow interaction did alter the vortex ring axis-switching frequency. This is because shear in the boundary layer can stretch the vortex ring while background vorticity complicates the vortex topology. In particular, the circulation around the ring becomes variable leading to branches in the vortex tube, which can present as hairpin legs or a trailing vortex loop [31,32]. Berk and Ganapathisubramni [33] detected similar vortex ring topologies in their PIV measurements of a rectangular orifice synthetic jet in a crossflow. To understand the cause of the momentum deficit behind the synthetic jet they employed a Biot-Savart law-based solver to model the vortex rings with their hairpin legs. The induced velocity on the jet centerline predicted by the model compared favorably with the phase-locked PIV data. Some of the remaining discrepancies between the measurements and model may partially be explained by the fact that the vortex ring was modeled as a circle and therefore did not capture the likely axis switching of the noncircular vortex rings produced by the AR = 13 rectangular orifice in the experiment. It will be shown that axis switching has a substantial effect on the induced velocity within moderate and high AR vortex rings.

In the present study experimental stereoscopic particle image velocimetry (SPIV) data were obtained for SJAs with rectangular orifices ranging in AR from 2 to 19. That range encompasses both small and moderate AR values and covers a larger sweep in AR than has been typically investigated in prior synthetic jet experimental studies. The processing of the SPIV data in this study was focused on elucidating the vortex dynamics associated with the different shape vortex rings in the jets. In addition, complementary Biot-Savart simulations were run to aid in interpreting the complex flow fields which enabled the origin of several features captured in prior studies to be explained in the context of the dynamics of the primary vortex structure. Accordingly, Sec. II will review the design parameters of the synthetic jet and the techniques used to acquire the experimental data, while the modeling approach is summarized in Sec. III. In Sec. IV the results are discussed,

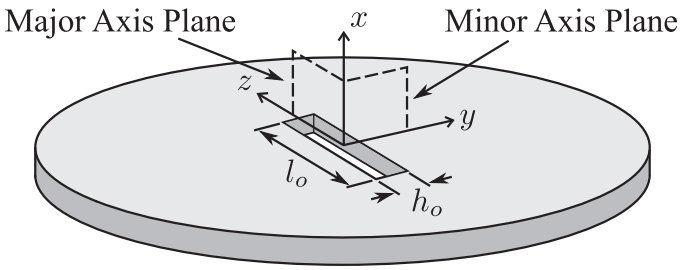

FIG. 2. Schematic detailing the synthetic jet orifice geometry and coordinate system utilized.

starting with a detailed look at the AR = 6 orifice jet and finishing with an examination of the similarities and differences seen in the other AR cases. Finally, a summary and the conclusions are presented in Sec. V.

II. EXPERIMENTAL METHODS

A. Synthetic jet

To study the effect of the orifice AR on the vortex dynamics in synthetic jets, a modular synthetic jet actuator with interchangeable orifice plates was designed and manufactured in house. The 71.1-mm-diam orifice plates contained the actuator orifice and were fabricated on a Formlabs Form 2 stereolithography three-dimensional (3D) printer using a black photopolymer resin. This technique enabled rapid prototyping of various orifice geometries while maintaining a high degree of part commonality in the actuator. In this study five orifice geometries were tested which covered a range of AR values, i.e., the ratio of the orifice length to its width ($AR_o = l_o/h_o$) (Fig. 2). Note that the dimensions associated with the jet orifice are denoted by a subscript o (e.g., h_o, l_o, and AR_o), while the dimensions associated with the vortex ring will have a subscript r (e.g., h_r and AR_r). To account for variability in the 3D printing process h_o and l_o were measured using a set of precision metric pins and calipers. The resulting dimensions of the five orifices yielded AR_o of 2.0, 4.0, 6.1, 12.6, and 19.3; however, from here on these are referred to as the cases of $AR_o = 2$, 4, 6, 13, and 19 for brevity. The length and width of the orifices were chosen to maintain a constant orifice exit area of 18 mm^2 across all of the cases tested. The neck height of the orifices, i.e., the orifice depth, was also held constant at 2.59 mm.

In addition to containing the orifice, the underside of the orifice plate also contained the actuator cavity. The piezoelectric disk used to drive the actuator was clamped against the orifice plate sealing the bottom of the cavity. The resulting cylindrical cavity had a height of 3.18 mm and a diameter of 58.42 mm. A single Piezo Systems bilayer piezoelectric bending disk actuator with a 63.5-mm-diam and maximum free deflection of ± 476 μm was used. The piezoelectric disk was driven with an Agilent 33500B series waveform generator in the continuous sinusoidal mode of operation and the input voltage was boosted with a Piezo Master VP7210 amplifier. Clamping of the piezoelectric disk against the orifice plate was achieved with two aluminum rings. These rings were held together by six screws that were installed with a torque wrench to precisely control the clamping force on the piezoelectric disk.

The coordinate system used for the synthetic jet flow field originates at the exit plane of the actuator in the center of the orifice (Fig. 2). The x coordinate aligns with the axis of the jet and increases in the streamwise or axial direction, while the y and z coordinates are aligned with the minor and major axes of the rectangular orifice, respectively. The orifice width h_o was chosen as the characteristic length for the flow. Finally, the flow velocity in the x, y, and z directions are labeled u, v, and w, respectively.

Several different characteristic velocity definitions have been put forth for synthetic jets over the years. In this study we opt to use the average orifice blowing velocity employed by Smith

TABLE I. Synthetic jet orifice dimensions and experimental conditions investigated.

AR_o	h_o (mm)	D_{eq} (mm)	U_o (ms^{-1})	Re	St	L_o/D_{eq}
2	2.95	4.74	11.0	2168	0.144	4.31
4	2.10	4.75	11.4	1595	0.099	4.45
6	1.71	4.75	11.6	1320	0.080	4.52
13	1.16	4.64	11.2	866	0.056	4.49
19	0.93	4.60	11.6	716	0.043	4.67

and Glezer [3] because it enables a more direct comparison with prior studies of the dynamics of piston-generated vortex rings. The average blowing velocity of a synthetic jet U_o is found by integrating the instantaneous velocity of the jet at the orifice $u_o(t)$ over the half of the actuator cycle that represents blowing divided by the period of the full cycle T, as defined by

$$U_o = \frac{1}{T}\int_0^{T/2} u_o(t)dt = fL_o. \tag{2}$$

If the jet velocity at the orifice varies in a sinusoidal manner with a frequency f, then the average blowing velocity is merely the peak speed U_p divided by π,

$$U_o = \frac{1}{T}\int_0^{T/2} U_p \sin(2\pi ft)dt = \frac{U_p}{\pi}. \tag{3}$$

The jet Reynolds number and Strouhal number were calculated using

$$\mathrm{Re} = \frac{U_o h_o}{\nu}, \tag{4}$$

$$\mathrm{St} = \frac{f h_o}{U_o}, \tag{5}$$

respectively, where ν is the kinematic viscosity of the fluid. Accordingly, the configurations and conditions of the five cases tested are summarized in Table I.

While researchers working on the application of flow control technologies generally favor Re and St when reporting experimental conditions, those focused on the study of vortex dynamics often report Re_Γ and L_o/D, i.e., the Reynolds number based on circulation and the dimensionless stroke length or stroke ratio. Here L_o is the stroke length of the actuator and is often defined in synthetic jets as the average blowing velocity divided by the actuation frequency (2). For jets or starting vortices formed from nonaxisymmetric orifices or nozzles that do not have a single length scale D, the equivalent diameter D_{eq} is used, which is the diameter of a circular orifice with the same exit area as the noncircular one [1]. Note that if St is computed using D_{eq} as the length scale, L_o/D_{eq} is merely the reciprocal of St [see Eqs. (2) and (5)]. While h_o was chosen as the length scale in this work, due its ubiquity in finite-span synthetic jet studies, L_o/D_{eq} can be a useful parameter when comparing the results in this study to prior work on vortex ring formation. Therefore, the stroke ratio and equivalent diameter of the orifice are reported in Table I.

As the stroke ratio of an actuator L_o/D_{eq} is increased the generated shear layer which feeds the forming vortex ring contains more circulation, leading to a stronger vortex [34]. There is a natural limit to this process, however, because when the vortex ring gets sufficiently strong its high self-induced velocity causes it to outrun the shear layer feeding it such that it pinches off from its source of vorticity. Therefore, there is an upper limit to the formation time and relative strength of a vortex ring formed in this manner. Experiments conducted with circular and low AR elliptic vortex rings have found that this limiting formation time or formation number falls in the range of $L_o/D_{eq} = 3.4$–4.5 [34,35]. For stroke ratios slightly above this limit the pinched-off vorticity tends to remain near the orifice or nozzle where it slowly dissipates or, in the case of synthetic jets,

may be reingested by the actuator during the suction phase. If the stroke ratio is well above the limiting formation number, however, the shear layer left behind contains sufficient vorticity to form secondary vortex rings which travel behind the primary ring [34,36].

In a companion study the influence of Re and L_o/D_{eq} (or St) on synthetic jet axis switching was investigated by analyzing the changes in the half-width of a rectangular orifice synthetic jet [29]. The shape of the jet was unaffected by variations in Re between 298 and 731; however, the stroke ratio did have an influence on axis switching. Specifically, axis switching was insensitive to the driving conditions when L_o/D_{eq} was below $\sim$4 but was sensitive for $L_o/D_{eq} > 4.2$. In the highest stroke length case ($L_o/D_{eq} = 6.2$) the pinched-off vorticity formed a secondary vortex ring which interacted with the primary vortex ring downstream, delaying axis switching. Conversely, at $L_o/D_{eq} = 4.2$ a small amount of pinched-off vorticity was observed, but it did not form a secondary ring, nor did it appear to influence the initial axis-switching deformations of the primary vortex ring. Because vortex pinch-off, specifically secondary vortex ring formation, is the primary factor influencing vortex ring axis switching in synthetic jets, in this study we sought to hold L_o/D_{eq} constant (Table I). We believe this is more appropriate when comparing axis switching between different AR orifices than holding constant Re or St, as computed using the length scale h_o. The actuator driving conditions were set at roughly the limiting formation number so that the primary vortex rings would have the maximum possible strength. This made the vortices easier to detect and analyze in the SPIV data and minimized the vortex rings' interaction times with the orifice. Although a vorticity tail was detected due to vortex pinch-off for the driving condition used in this study, it will be shown that this tail was too weak to form a secondary vortex ring and instead remained close to the orifice where it was at least partially reingested during the suction phase.

B. Thermal anemometry

The resonant frequency of the synthetic jet actuator and the maximum orifice exit air speed at resonance was determined using a thermal anemometer, commonly referred to as a hot wire. These measurements were collected using an A.A. Lab Systems AN-1003 constant-temperature anemometer system with a Dantec miniature single-component hot-wire probe. The hot-wire probe was calibrated in the potential core of a calibration jet over a velocity range of $0.1 < U < 55$ ms^{-1}. Hot-wire measurements were then made with the probe inserted into the SJA orifice to half the neck height, on its centerline, for a range of driver frequencies. Data were recorded at 50 kHz or roughly 80–100 points per cycle, depending on the synthetic jet actuator driving frequency. The peak speed measured in the orifice was approximately 36 ms^{-1} for all five orifices. The maximum air speed was achieved at an actuator driving frequency of 540 Hz and this frequency was used for all subsequent SPIV measurements.

C. Stereoscopic particle image velocimetry

The velocity field within the jet was measured using SPIV. The SPIV experiments were conducted in a $61 \times 61 \times 76$ cm^3 ($24 \times 24 \times 30$ in^3) quiescent enclosure which isolated the test environment from air currents in the laboratory. The enclosure was constructed using 3.18-mm-thick ($\frac{1}{8}$-in.-thick) cell cast acrylic panels on four sides to provide low-distortion optical access in a number of test configurations. The enclosure was seeded with incense smoke for the SPIV experiments. The synthetic jet device was mounted on two Velmex linear traverses in a y-z configuration which allowed for precise adjustments to the location of the jet with respect to the fixed SPIV measurement plane.

Stereoscopic PIV was utilized to map out the spatial development of the vortex rings in the synthetic jet and to determine the height of vortex ring axis switching. The measurements were collected with a LaVision SPIV system comprising two 2560×2160 pixel 16-bit dynamic range scientific CMOS cameras capable of 50 frames/s. A Quantel Evergreen 200 dual-pulsed 532-nm Nd:YAG laser, with a -50 mm focal length cylindrical lens to spread the beam into a sheet, provided

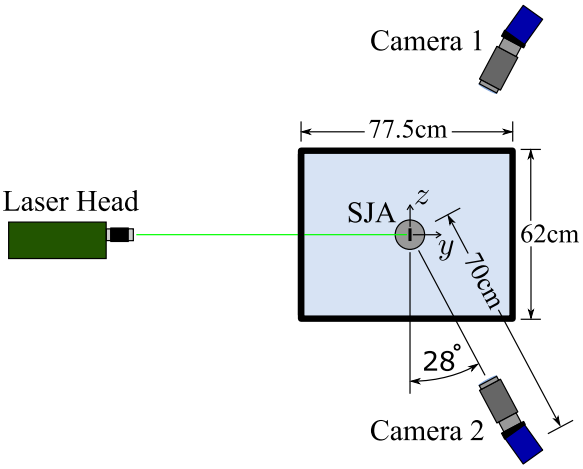

FIG. 3. Schematic detailing the experimental setup of the synthetic jet actuator, enclosure, and SPIV system.

illumination of the particles within the enclosure. A second set of adjustable optics was used to focus the width of the sheet to a minimum waist above the orifice of the synthetic jet. The bottom of the light sheet was clipped at $x \approx 1$ mm above the orifice surface before the light entered the quiescent enclosure to eliminate surface reflections in the images. The laser was positioned so that the light sheet illuminated an imaging plane which bisected the orifice along its centerline. The two cameras were set up on either side of the quiescent enclosure angled 28° from the normal of the imaging plane in a forward scattering orientation (Fig. 3). Each camera was fitted with a Nikon Nikkor 200-mm macro f/4D lens connected to a LaVision Scheimpflug mount which was adjusted to get the full width of the imaging plane in sharp focus. The resulting image scale factor was 49 pixels/mm. The positioning of two cameras at an angle to the imaging plane enabled the three-component velocity field in that plane to be computed by stereo cross correlation of the particle displacements.

Stereoscopic PIV measurements were collected in the x-y and x-z planes of the orifice by rotating the entire synthetic jet actuator assembly 90° while keeping the laser and cameras fixed (Fig. 3). The x-y and x-z centerline planes bisect the orifice along its two planes of symmetry and will be referred to from now on as the minor axis plane and major axis plane, respectively (Fig. 2). This orifice relative terminology will be used irrespective of the vortex ring orientation, which periodically changes due to axis switching. In both planes, six to seven phase-locked sets of 500 image pairs were recorded at a range of phase angles in the actuation cycle. Additionally, a single 500-image set was recorded in both planes at a frequency selected to randomly cause aliasing with the synthetic jet driving frequency for the purpose of obtaining the time-averaged (i.e., mean) field. The raw images were processed using LaVision's DaVis software (version 8.4.0) to find the three-component planar velocity field (i.e., 2D3C). The stereo cross correlation was computed using a multipass method with two passes on 64×64 pixel interrogation windows followed by a single pass on 32×32 pixel windows. A Gaussian weighting function was applied to the interrogation windows and a 50% overlap was used between windows. The data processing yielded a 152×150 vector field, accounting for the masking at the edges of the frame.

The measurement uncertainties associated with the three velocity components obtained via SPIV were estimated using the correlations statistics method implemented in DaVis and described in Ref. [37]. To summarize the results across the vector field, the root-mean-square (rms) of all the individual vector uncertainties was taken within the jet, i.e., in the region where $u(x, y) > 0.01u_{\max}(x)$. Restricting the rms to the measurements inside the jet resulted in more consistent uncertainty values across the various jet AR values tested and is more conservative than including the region outside

TABLE II. Estimated uncertainty in SPIV measurements reported as the root mean square of the uncertainty field within the jet. Ranges cover the minimum to maximum uncertainty observed for all actuator phase angles and AR values measured.

	Major axis plane		Minor axis plane	
Uncertainty	Phase-locked	Time-averaged	Phase-locked	Time-averaged
σ_u^{rms}/U_o	0.41–0.87%	0.95–1.42%	0.57–0.94%	0.88–1.82%
σ_v^{rms}/U_o	0.38–0.75%	0.62–0.92%	0.55–0.96%	0.65–1.05%
σ_w^{rms}/U_o	0.38–0.77%	0.53–0.86%	0.49–0.84%	0.60–1.00%

the jet where uncertainty is generally lower. Furthermore, reporting the rms value is consistent with the convention used in prior studies of PIV uncertainty quantification [37]. The rms measurement uncertainties in u, v, and w for the phase-locked and time-averaged measurements in the major axis (x-z) and minor axis (x-y) planes for all phases and AR values tested are reported as ranges in Table II.

Postprocessing of the vector files was conducted in MATLAB to establish the shape and location of the vortex rings emitted by the synthetic jet actuator. Vortices were identified using the Q criterion in positive regions of the Q field where rotation dominates strain [38,39]. For vortex identification a threshold was applied to the Q field at a level above zero. The location of the peak vorticity ω within the region enclosed by the Q contour at the threshold level was then interpolated to extract the vortex core axis. Finally, the vortex locations in the two orthogonal measurement planes were used to reconstruct the three-dimensional geometry of the vortex ring.

III. MODELING APPROACH

Numerical solutions to the Biot-Savart law equation are relatively easy to obtain and computationally inexpensive compared to today's commonly used higher-order methods (e.g., unsteady Reynolds-averaged Navier-Stokes and large-eddy simulation models). Although this method is unable to model viscous processes like vortex formation and decay, it will be shown that the Biot-Savart law is able to qualitatively capture many aspects of noncircular vortex ring dynamics in a synthetic jet.

An inviscid Biot-Savart solver called IBiSS was developed in MATLAB to conduct this analysis. Results from IBiSS are presented in this paper to give additional insight into the dynamics captured in the SPIV data. The vortex rings were modeled as finite span, bilaterally symmetric rings with a specified AR. The initial geometry of the vortex ring consisted of two parallel line segments running along either side of the major axis joined by semicircular ends of radii $r/h_r = 0.5$ which spanned the minor axis (see the t_0 geometry in Fig. 1). Kiya *et al.* [40] employed the same vortex ring geometry in their vortex blob simulations and referred to it as pseudoelliptical. The 3D flow field reconstructions experimentally obtained by Straccia and Farnsworth [29] for an AR = 13 synthetic jet reveal that this pseudoelliptical shape is a reasonable approximation of the vortex ring formed in moderate AR rectangular orifice synthetic jets [see Fig. 19(a) in [29], for example]. A few limited studies were conducted with IBiSS to investigate the effect of the radii at the "corners" of the vortex ring on the self-induced dynamics. When the corner radii are reduced ($r/h_r < 0.5$) to give the ring a slightly rounded-off rectangular shape the sharper corners introduce higher-order azimuthal modes into the ring's deformation but do not substantially influence the axis-switch height. The fluctuations associated with the higher-order azimuthal modes in the sharper cornered vortex rings also cause the ring width in the major and minor axis planes to oscillate relative to the pseudoelliptical ring solution, but these differences are oscillatory not divergent. It was concluded that the corner radius of the ring does not have a first-order effect on the self-induced deformations; therefore, all of

the simulations presented in this paper employed an initially pseudoelliptical vortex ring shape ($r/h_r = 0.5$).

To input the vortex ring geometry into the solver, the ring axis was discretized into a series of line segments which were specified by the coordinates of their end points (vertices), with the first and last line segments sharing a common end point to ensure closure of the ring. The number of line segments was defined in the widthwise direction and varied in the lengthwise direction with the ring AR to maintain approximately equal initial line segment lengths Δs around the ring. In the majority of the analyses presented, a line segment density of $\sim$15 segments per vortex length h_r was used. In an $\mathrm{AR}_r = 6$ vortex ring this line segment density corresponds to a total of 200 line segments throughout the ring. Some limited results will be discussed which utilize different line segment densities to explore the dependence of the solution on the vortex ring geometric resolution.

IBiSS also requires the circulation strength of the vortex ring as a simulation input. While circulation has a direct influence on the celerity of the vortex ring (i.e., its temporal development) it does not affect the spatial development. In other words, in an inviscid simulation a vortex ring with twice the circulation strength but the same shape as a weaker vortex ring will undergo the same deformations at the same points in space as the weaker one; it will just do so more quickly. With one exception, the results reported from IBiSS relate to spatial parameters like axis-switch height and vortex ring width; therefore, circulation strength of unity was used for the duration of the simulations. At the end of Sec. IV a comparison between experimental data and an IBiSS simulation employing variable vortex ring circulation strength will be discussed in more detail.

In the solution approach, the induced velocity at all of the vortex ring line segment vertices is computed at the current time step using the Biot-Savart law (1). The position of the vortex ring in the subsequent time step is then found using the modified Euler approach outlined by Hama [41]. This multistep technique has superior stability compared with the conventional Euler method. To maintain stability of the explicit time-marching integration the time step size Δt must be small enough to satisfy the Courant-Friedrichs-Lewy (CFL) condition, as expressed in terms of circulation strength Γ,

$$C_{\max} \geqslant \frac{\Gamma \Delta t}{(\Delta s)^2}. \tag{6}$$

By trial and error a maximum Courant number $C_{\max}$ of 0.2 was found to be a reliable stability limit for the modified Euler scheme in the context of Biot-Savart modeling. Furthermore, when the time step size was set small enough to satisfy the CFL condition the resulting spatial development of the vortex ring was confirmed to be independent of the time step size. Accordingly, the time step size was selected so that the Courant number was between 0.02 and 0.12 for all of the simulations.

IBiSS has the ability to include an image vortex in a simulation to model the effect of the wall around the orifice, but in the present case there are challenges in doing so accurately. Specifically, the image effect is only appreciable when the vortex is close to the wall, i.e., while the vortex is forming. However, during the formation phase the vortex circulation is rapidly changing and therefore an accurate variable circulation profile is required all the way down to the wall. There is also a distinct difference between the motion of the vortex ring during formation, which is strongly influenced by the motion of the fluid slug and roll-up of the shear layer, and the later inviscid advection phase, which is dominated by self-induction [42]. Therefore, to correctly model the image vortex effect, detailed data on the motion and circulation of the vortex ring during formation would be required. A method would also be required for estimating an appropriate offset height from the wall at which to start the simulation. A further complication with synthetic jets is that the suction phase of the actuator likely disrupts the blocking effect of the wall later in the cycle.

The primary effect of the image vortex is to cause the primary vortex ring to shrink in width and length at the very beginning of a simulation. This shrinkage in diameter or width near the orifice or nozzle has been captured experimentally and it quickly asymptotes to a stable value as the ring propagates away [42–44]. Effectively this is the reverse of the classic vortex ring–wall collision interaction. The smaller vortex ring deforms more quickly than a vortex formed without an image

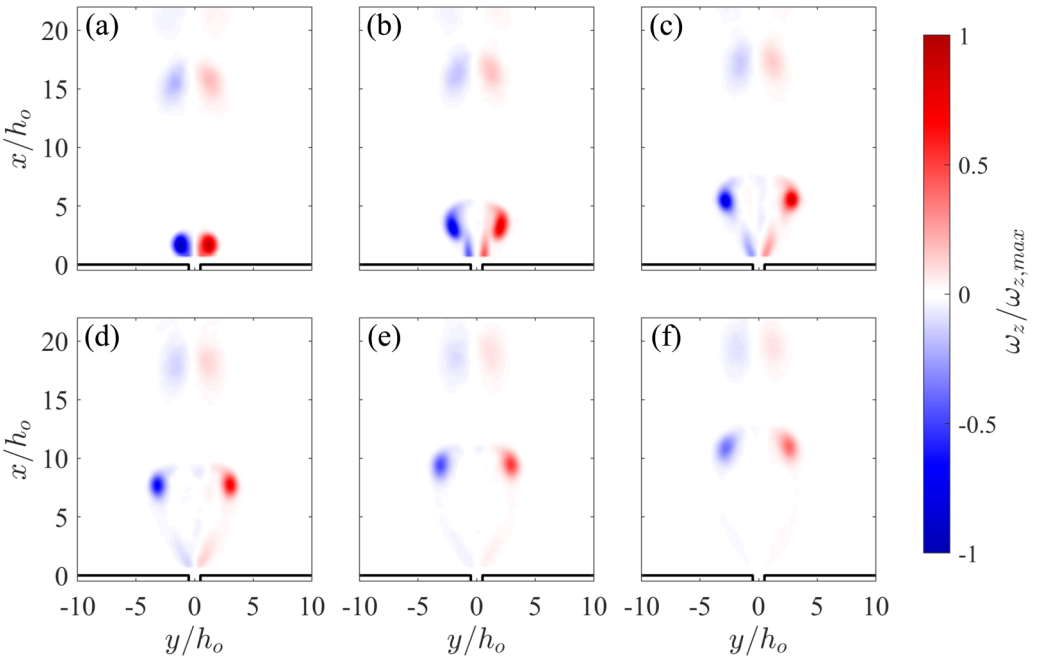

FIG. 4. Contours of normalized phase-locked vorticity in the minor axis plane of the $AR_o = 6$ synthetic jet for phase angles (a) 103°, (b) 143°, (c) 183°, (d) 223°, (e) 263°, and (f) 303°.

causing spatial parameters like the axis-switch height to be reduced. However, this change in the spatial development of the vortex ring can be largely eliminated by scaling by the initial vortex ring width h_r, as is done later in this paper when comparing the axis-switch height from SPIV data to IBiSS simulations. Due to the complexities of accurately modeling the image vortex effect during the vortex formation phase and the fact that proper scaling of spatial parameters essentially obviates the image vortex, this feature was not included in the reported simulations. Furthermore, the simulations begin with the vortex at a height of $x = 0$ without any type of formation offset correction.

IV. RESULTS

A. Vortex dynamics in an AR = 6 orifice synthetic jet

To demonstrate the effect axis switching has on the shape and trajectory of the vortex rings in a synthetic jet, six phase-locked vorticity fields from the $AR_o = 6$ case are presented in the minor axis (Fig. 4) and major axis planes (Fig. 5). The phase angle of the jet at the orifice exit is reported relative to the start of the blowing cycle such that 0°, 90°, 180°, and 270° correspond roughly to the start of blowing, the point of peak blowing, the start of suction, and the point of peak suction, respectively. The relative position of the first measured phase within the jet cycle is accurate to ±5° and the following data sets are spaced every 40°. Furthermore, the colormap used here, and in similar upcoming figures, represents regions of negative vorticity in blue, regions of positive vorticity in red, and areas with little to no rotation in white, according to the right-handed convention. In each panel two to three generations of vortex rings are identifiable as antisymmetric pairs of concentrated vorticity. The vortex rings form at the bottom of the frame and travel upward in the positive x direction while deforming due to the axis-switching oscillations. Note that while a small amount of vorticity pinches off from the newly formed vortex ring [Figs. 4(c) and 5(c)], this weak tail remains near the orifice and is at least partially reingested by the actuator during the suction phase [Figs. 4(f)

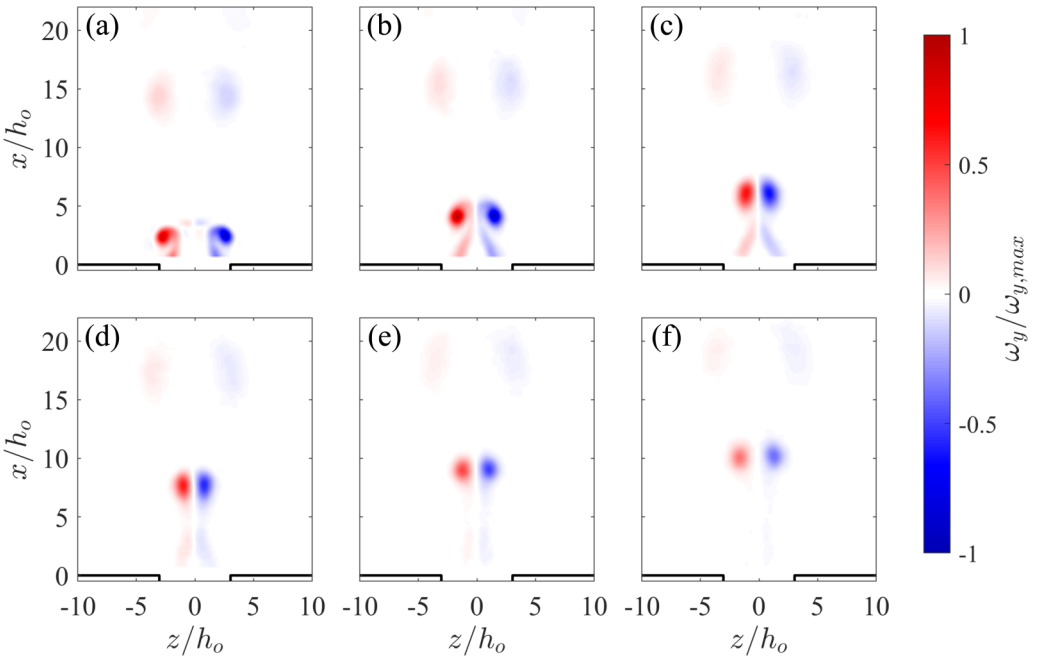

FIG. 5. Contours of normalized phase-locked vorticity in the major axis plane of the $AR_o = 6$ synthetic jet for phase angles (a) 103°, (b) 143°, (c) 183°, (d) 223°, (e) 263°, and (f) 303°.

and 5(f)]. Therefore, the pinched-off vorticity does not interact with the vortex ring downstream. To visualize the relative changes in the vortex ring shape and position, it is convenient to consolidate the data from the various phase angles into a single figure as presented in Fig. 6.

The distinct effect vortex ring axis switching has on the shape of synthetic jets is plainly visible in the time-averaged vorticity contours on the two centerline planes of the $AR_o = 6$ jet (Fig. 6). The vorticity streaks in the time-averaged contours provide a history of the paths of the vortices in

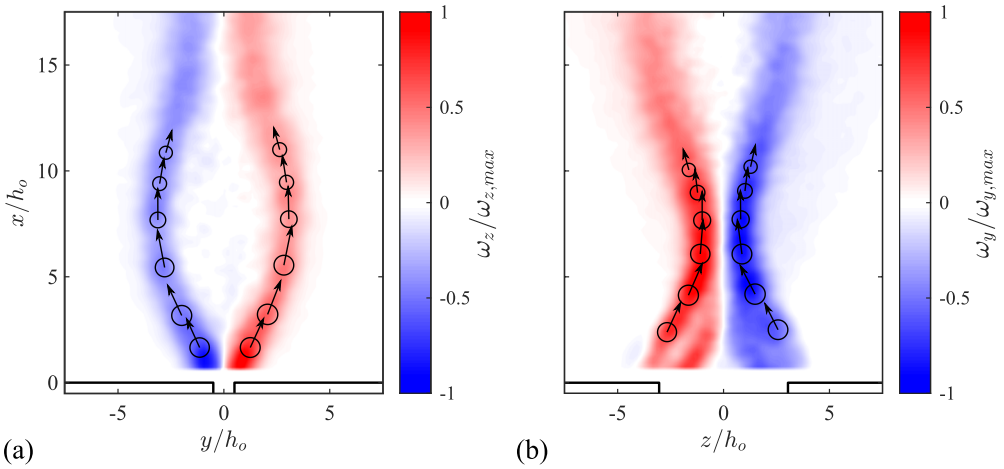

FIG. 6. Contours of normalized time-averaged vorticity in (a) the minor axis and (b) the major axis planes overlaid with phase-locked vortex locations (circles) and velocities (vectors) in the $AR_o = 6$ synthetic jet.

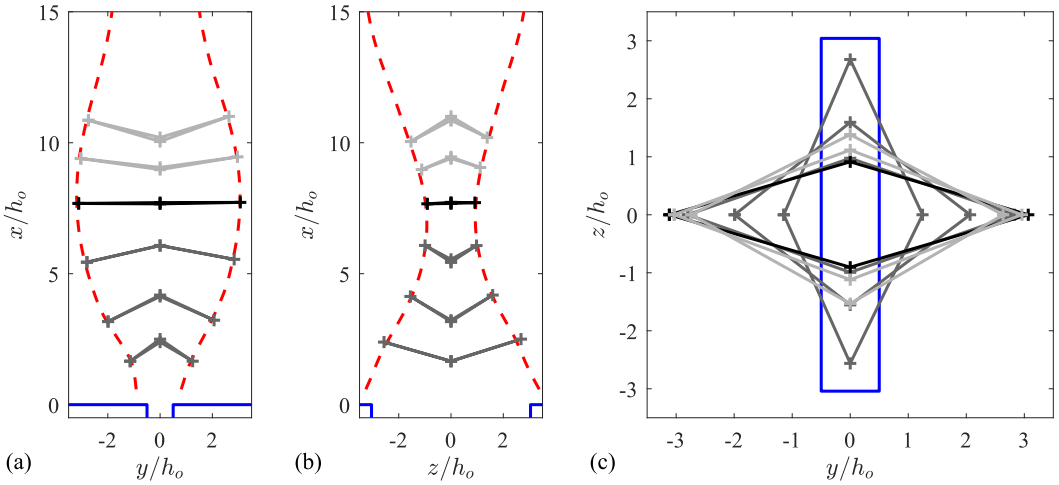

FIG. 7. Phased-locked vortex ring locations (pluses) and time-averaged vortex paths (dashed curves) in (a) the minor axis plane, (b) the major axis plane, and (c) the top view for the $AR_o = 6$ synthetic jet.

that plane as they travel away from the actuator. Overlaid on the filled contours are black circles indicating the positions of the vortices at six evenly spaced phases of the jet which are separated by 40° increments of the actuation cycle. The radii of the circles are scaled by the magnitude of the vortex circulation strength at that phase. In addition, vectors originating from the circles' centers represent the direction of the phase-locked velocity at the vortex axis, while the lengths of the vectors are scaled by the flow speed.

In the minor axis plane the initially narrow jet starts to spread outward a short distance downstream of the orifice [Fig. 6(a)]. The direction of the velocity at the vortex centers reveals how vortex ring self-induction drives the rapid spreading of the jet. Further downstream in the jet the spreading slows and the jet achieves a maximum width at $x/h_o = 8.1$. The jet begins to contract downstream of $x/h_o = 8.1$, which is mirrored in the inward pointing velocity vectors for the last two vortex phases. The contraction of the vortex rings and the jet in the minor axis plane continues until a height of $x/h_o = 16.9$, where a local minimum is achieved.

The behavior of the $AR_o = 6$ jet in the major axis plane [Fig. 6(b)] is roughly the inverse of what was observed in the minor axis plane. The wide axis of the jet contracts initially as the self-induced velocity from the vortex ring drives the vortices towards the centerline, and at a height of $x/h_o = 7.0$ the jet reaches a minimum width. Downstream of $x/h_o = 7.0$ the velocity vectors at the vortex centers tilt outward, away from the jet centerline, and the jet expands again.

In both measurement planes the vortex ring starts to deform while the vortex is still accumulating circulation, as indicated in Fig. 6 by the increasing radii of the circles marking the vortex locations. Vortex circulation strength peaks around the second or third phase plotted and as a result the self-induced velocity is also highest at these phases. In the final three phases the vortex strength slowly decays, as the does the vortex speed, evidenced by the shorter distance traveled during each time increment by the later vortices.

To visualize the self-induced deformation of the vortex ring, the phase-locked vortex locations were reconstructed into a rough representation of the ring (Fig. 7). The same six evenly spaced phases of the actuator from Fig. 6 are presented again. The four vortex locations extracted from the two centerline planes at a particular phase are indicated with pluses connected by straight lines. In addition to the phase-locked results, the vortex locations in all 500 individual vector fields, which constitute the time-averaged data set, were also extracted and fit with spline curves. These spline curves are plotted as two red dashed curves in Figs. 7(a) and 7(b). Finally, the position and size of the orifice are indicated at $x/h_o = 0$ in blue.

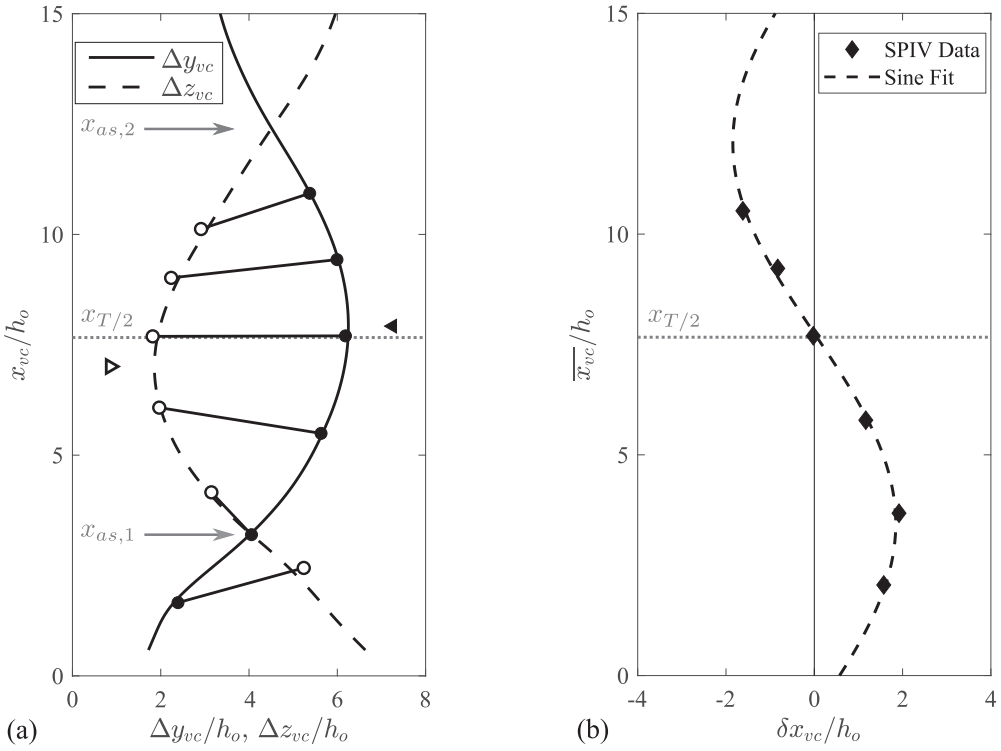

FIG. 8. Axial variation of (a) vortex ring width in the major axis (dashed curve) and the minor axis (solid curve) planes and (b) height difference between vortices in the major and minor axis planes for the $AR_o = 6$ synthetic jet.

Despite the coarse representation of the vortex rings from the SPIV data (Fig. 7), it is apparent that the deformations of the physical ring develop in a manner similar to what was predicted by IBiSS (Fig. 1) and described in Sec. I. The vortex ring returns to a roughly planar configuration with the axes switched at a height of $x/h_o = 7.7$, where the fourth phase of the ring presented in Fig. 7 approximately corresponds to t_4 in Fig. 1. Above $x/h_o = 7.7$ the axis-switching deformations continue, as seen in the final two phases, and although it is not captured in this figure, eventually the vortex ring returns to its original orientation further downstream.

The difference in the vortex ring's position in the major and minor axis planes of the $AR_o = 6$ jet is presented in Fig. 8. Figure 8(a) displays how the width of the vortex ring changes in the minor axis (Δy_{vc}) and major axis (Δz_{vc}) planes as the ring propagates downstream. The dashed and solid curves represent the distance of separation between the two spline curves that were fitted through the instantaneous vortex locations [see the red dashed curves in Figs. 7(a) and 7(b)]. These curves highlight that the undulations in the jet widths are roughly 180° out of phase between the two planes. The vortex separation distances in the six phase-locked data sets are also presented as closed (minor axis plane) and open (major axis plane) circles connected by solid lines. In addition, the height at which the vortices in the major axis plane reach a minimum width is indicated by an open triangle, while the height of the maximum width in the minor axis plane is indicated by a closed triangle. Interestingly, the vortex rings do not achieve their minimum width in the major axis plane at the same downstream distance from the orifice as the vortices in the minor axis plane achieve their maximum separation. A similar phenomenon has been observed in isolated vortex rings [19,22].

One measure of axis switching, which has been used in prior studies of nonaxisymmetric jets, is the jet axis-switch height. As the jet grows in width in one plane and shrinks in width in the

other, eventually a crossover point is reached where the widths in the two planes are equal. The jet axis-switch height, which we denote by x_{as}, is the streamwise distance above the orifice where this crossover occurs [16]. This axis-switch height is traditionally based on the width of the jet as determined using the half-velocity point $y_{1/2}$, where $u(x, y_{1/2}) = U_{\max}(x)/2$, i.e., the point away from the jet centerline where velocity has decayed to a half the maximum velocity value from that height. We will refer to this measure of the jet width as the velocity width. In this study, that technique for finding the crossover height is compared to the crossover height identified using the paths of the vortex centers from the time-averaged data sets. The jet axis-switch heights based on the vortex paths can be identified in Fig. 8(a) as the points where the dashed and solid curves cross, i.e., $x_{as,1}/h_o = 3.2$ and $x_{as,2}/h_o = 12.4$. The width of the jet based on the vortex paths will be referred to as the vortex trajectory width. It should be noted that from a vortex dynamics perspective, the axis-switch height has little significance since the vortex ring does not possess those two dimensions [i.e., $\Delta y_{vc}(x_{as})$ and $\Delta z_{vc}(x_{as})$] at the same time. Furthermore, the height at which the vortex ring actually has equal widths along its two axes is not necessarily the same as when the jet has equal widths (e.g., see phase-locked data in Fig. 8 herein and Fig. 4 in [22]).

If we treat axis switching as a periodic oscillation of the vortex ring geometry, then the point at which the ring achieves a roughly planar shape, but with the axes flipped relative to the start of the cycle, is approximately the half-period point (see the t_4 vortex ring in Fig. 1 and the black vortex ring in Fig. 7). We view this point as the completion of the first axis switch and propose it as a more relevant measure of the axis switching from the perspective of the vortex dynamics. The height at which the first axis switch is completed will be denoted $x_{T/2}$. The second time that the vortex ring achieves a roughly planar shape, but now with major and minor axes in the same orientation as at the start of the cycle, marks one period of the cycle. This point marks the completion of the second axis switch and the height where it occurs is denoted by x_T. For reference, the heights of the *jet* first and second axis switches ($x_{as,1}$ and $x_{as,2}$) occur at roughly the quarter-period and three-quarter-period of the vortex ring axis-switching cycle, respectively.

Identifying the height at which the vortex ring returns to a roughly planar configuration involves analyzing a discrete set of phase-locked measurements. An iterative data acquisition approach could be used to identify the phase when the vortex ring completes the axis switch; however, modeling conducted with IBiSS revealed a simpler way of determining the $x_{T/2}$ point. The two measurement planes (x-y and x-z) intersect the vortex ring axis at four points. Two of these points span the major axis of the vortex ring and the other two span the minor axis. As the vortex ring undergoes axis switching, the set of vortices that is further downstream periodically switches. Analysis of axis switching using IBiSS revealed that the difference in the vortex downstream positions between these four points varies in space in a predominantly sinusoidal manner, at least for low AR vortex rings. This dynamic attribute was utilized during the experimental investigation to limit the number of data points required to identify the height of the axis-switch half-period point.

In Fig. 8(b) the differences in the heights of the vortex centers in the minor versus the major axis planes, $\delta x_{vc} = x_{vc}(y = 0) - x_{vc}(z = 0)$, for the six phase-locked data sets are plotted using diamonds. Visually, δx_{vc} is the difference in height between the closed and open circles in Fig. 8(a), where positive δx_{vc} indicates that the vortex axes in the major axis plane are further downstream than the vortices in the minor axis plane, while negative δx_{vc} indicates the opposite. In Fig. 8(b) the vertical axis of the plot is now the average of the vortex heights in both the minor and major axis planes, $\overline{x_{vc}}$, which is roughly equivalent to the average height of the vortex ring. Initially, the vortices in the major axis plane are further downstream than those in the minor axis plane; however, this relationship flips above $\overline{x_{vc}}/h_o = 7.7$ as the axis switching continues. When δx_{vc} achieves a value of zero the major and minor axes of the vortex ring are coplanar and the full vortex ring is roughly planar. The height where the flatness deviation of the vortex ring is minimum is very near, if not coincident with, the height where $\delta x_{vc} = 0$, according to IBiSS simulations. The sine curve which was fit to the phase-locked data is plotted as a dashed line in Fig. 8(b). As predicted by IBiSS, the variation in δx_{vc} is essentially sinusoidal. The height of the sine curve crossing, $\Delta x_{vc} = 0$, was interpolated to find the half-period point of the vortex ring axis-switching cycle, $x_{T/2}$. For the

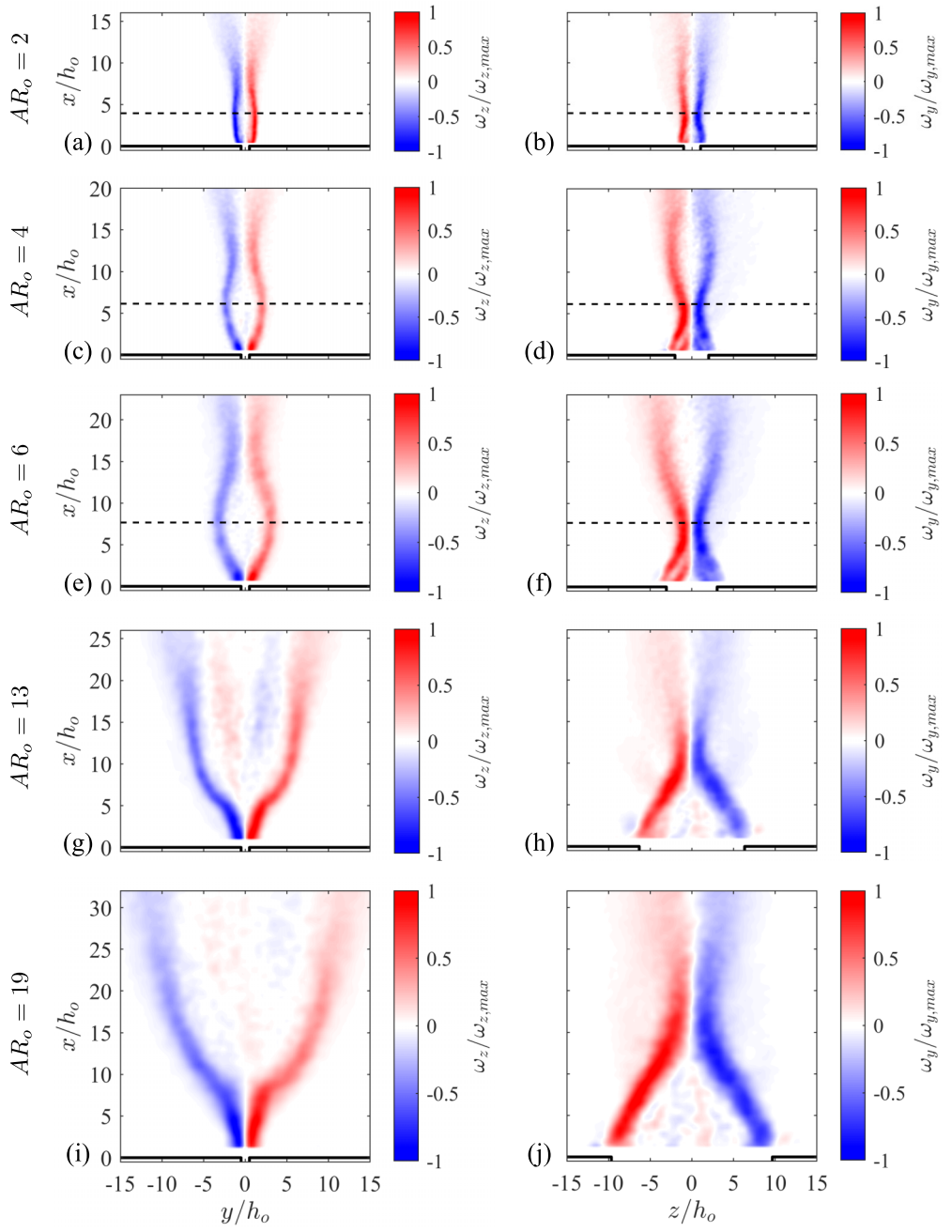

FIG. 9. Contours of time-averaged normalized vorticity in the (a), (c), (e), (g), and (i) minor axis plane and (b), (d), (f), (h), and (j) major axis plane for (a) and (b) $AR_o = 2$, (c) and (d) $AR_o = 4$, (e) and (f) $AR_o = 6$, (g) and (h) $AR_o = 13$, and (i) and (j) $AR_o = 19$. The axis-switching half-period height is indicated with a dashed line in (a)–(f).

$AR_o = 6$ case this yielded a value of $x_{T/2}/h_o = 7.7$. This height is marked in Figs. 8(a) and 8(b) with a horizontal dotted line.

B. Effect of AR on the vortex dynamics in synthetic jets

The time-averaged vorticity fields for all five orifice AR values tested are presented in Fig. 9 on the two centerline planes. The behavior of the jet is similar in three lowest AR orifices. Specifically, the jet initially grows in width in the minor axis plane and contracts in the major axis plane. The jet widths in the two planes reach extrema around the height where the first axis switch completes, $x_{T/2}$, indicated by a horizontal dashed line. Above $x_{T/2}$ the roles reverse and the jet grows in the major axis plane and contracts in the minor axis plane. Thus, axis-switching deformations of the vortex rings continue through more than one complete switch. Evidence of the second completed axis switch of the vortex rings is apparent further downstream in Figs. 9(a), 9(c), and 9(e).

A few trends are apparent as the AR of the orifice is increased. The first is that the oscillatory variations in the jet's width become larger as the AR of the ring increases. Larger AR vortex rings experience more exaggerated self-induced deformations as they propagate than do vortex rings which deviate only slightly from a circular shape. Another observed change is in the behavior of the early vortex ring in the minor axis plane [Figs. 9(a), 9(c), 9(e), 9(g), and 9(i)]. At $AR_o = 2$ and 4 the spreading in the width of the jet in this plane appears to start immediately. However, starting at $AR_o = 6$, it is apparent that the vortices travel a short distance almost straight downstream before spreading apart and this delay becomes more pronounced as the AR_o is increased further to 13 and 19. In high AR vortex rings the middle of the ring is far removed from the influence of the highly curved ends. This causes the middle of the ring to behave like a 2D vortex pair for some distance downstream until the deformations which are initiated at the ends of the ring are transmitted to the middle. The higher the ring AR is, the longer it takes for this disruption of the 2D behavior to occur.

The starkest difference between the lowest and highest AR jets tested occurs in the downstream half of the vorticity fields presented in Fig. 9. While the $AR_o = 2$, 4, and 6 results indicate that the vortex rings continue axis-switching deformations after the first axis switch has completed, this is not the case at $AR_o = 13$ and 19. Instead of reaching a maximum width and then contracting in the minor axis plane, the $AR_o = 13$ and 19 jets continue to widen, albeit at a slower rate. When the calculation displayed in Fig. 8(b) to find $x_{T/2}$ was performed on the $AR_o = 13$ and 19 jets, the results revealed that the vortex ring axes never recover a coplanar configuration and therefore the vortex rings do not technically complete their first axis switch. An explanation for why the periodic axis-switching deformations ceased can be found by analyzing the minor axis plane phase-locked vorticity contours for the $AR_o = 13$ synthetic jet [Fig. 10(a)]. Near the orifice, at a height of $x/h_o = 3$, a single pair of counterrotating vortices associated with the most recently formed vortex ring is seen. Further downstream however, at a height of $x/h_o = 17.5$, four vortices in two counterrotating sets exist. This particular vortex pattern indicates that the older vortex ring has bifurcated, i.e., split into two smaller vortex rings [29].

When noncircular vortex rings axis switch they do not fully recover their original shape by the completion of the axis switch. For elongated vortex rings, like the ones formed from a rectangular orifice, the ring develops a pinch at the middle [visible in Fig. 1(b) at t_4]. This pinch becomes more pronounced with increasing AR. When antiparallel vorticity from the two sides of the vortex ring come in contact, vorticity reconnection occurs [45]. The two inner vortices in Fig. 10(a) (labeled B) are bridge vortices formed from the coalescence of the reconnected vorticity. If enough circulation is transferred from the colliding midsection of the vortex ring to the bridge vortices, then the vortex ring bifurcates. Circulation was computed in the various parts of the vortex ring in the $AR_o = 13$ jet by integrating the phase-locked velocity fields around polygons which were manually drawn to encompass the full vortex while excluding adjacent vortices and secondary structures. That analysis revealed that roughly 53% of the vortex ring's circulation was transferred from the vortices which collided in the major axis (x-z) plane to the pair of bridge vortices which straddle the contact zone. This interpretation of the $AR_o = 13$ synthetic jet draws heavily on the work reported by Straccia and

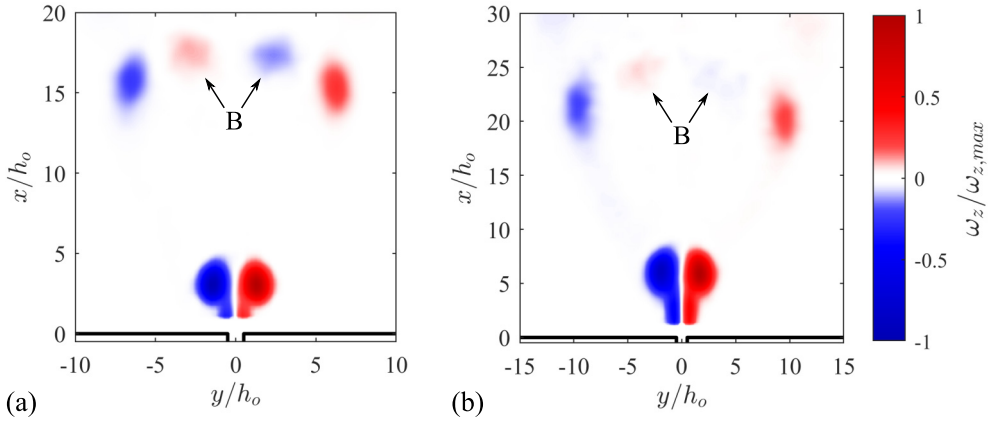

FIG. 10. Phase-locked normalized vorticity in the minor axis plane of the (a) $AR_o = 13$ and (b) $AR_o = 19$ jets. Bridge vortices are indicated by the B annotation.

Farnsworth [29], which employed the same actuator with an equivalent orifice and similar operating conditions.

The vortex ring formed by the $AR_o = 19$ orifice also shows evidence of vorticity reconnection but the bridges are less well defined than in the $AR_o = 13$ jet [Fig. 10(b)]. It was observed that the flow field around the vortex ring was more complex just prior to bifurcation in the $AR_o = 19$ case. However, the additional flow features which appeared within the vortex ring were quite weak and the vorticity field somewhat ambiguous; thus nothing definitive can be said regarding their origin. Instead, we mention this potential change in the vortex ring breakup mode to highlight an area that may be worthy of future study, particularly to investigate additional AR values and driving conditions.

In both the $AR_o = 13$ and 19 cases, the bifurcation of the vortex rings prevents further axis switching of the ring, as has been observed in continuous jets [1]. Careful inspection of the $AR_o = 6$ jet phase-locked vorticity fields revealed that vorticity reconnection was present in that case too [see regions of weak counterrotating vorticity between the primary vortices in Fig. 4(c)]. However, the amount of circulation transferred by vorticity reconnection in the $AR_o = 6$ case did not meet the minimum threshold required for bifurcation. Such vorticity reconnection without vortex ring bifurcation has also been reported in moderate AR isolated vortex rings and does not prevent further axis switching of the ring [22,23].

A survey of prior simulations and experiments investigating vortex ring bifurcation in isolated vortex rings reveals that the critical AR_r above which bifurcation occurs is roughly 4–5 [29]. To enable a comparison with this limit, the AR of the vortex rings from the different orifices were estimated by extracting the paths of the vortex centers identified in the instantaneous velocity fields of the time-averaged data sets. For the $AR_o = 6$ case these vortex paths are presented as red spline curves in Figs. 7(a) and 7(b). The vortex ring length was determined near the orifice by calculating the cross-stream distance between the clockwise and counterclockwise rotating vortex paths in the major axis plane. The vortex ring width was obtained in the same way in the minor axis plane. The ratio of the vortex ring length and width near the orifice provided an estimate of the initial AR_r. However, the lack of SPIV for the first 1 mm above the orifice, due to laser sheet cutoff, prevented an accurate assessment of the AR_r at the earliest point in its formation. Instead, the measurement bias in the present data was corrected based on a comparison with results from a later study conducted by the authors where data had been obtained closer to the orifice. The vortex ring from the $AR_o = 6$ orifice is projected to have $AR_r = 4.2$, at or slightly below the critical AR

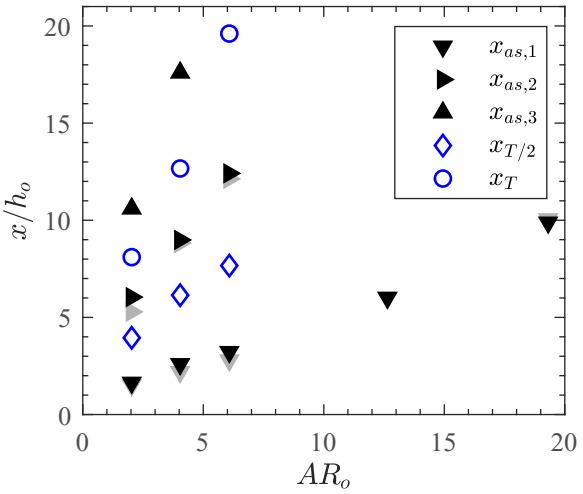

FIG. 11. Variation of axis-switching height (closed symbols) with AR_o as computed using jet velocity width (gray symbols) and vortex trajectory width (black symbols) in addition to the height of the axis-switching half period (open diamonds) and full period (open circles).

for bifurcation. Conversely, the vortex rings from the $AR_o = 13$ and 19 orifices have projected AR_r of 7.9 and 12.8, respectively, which are well above the critical limit.

C. Effect of AR on axis-switch height

In Fig. 9 it is also apparent that as AR_o is increased, the height at which the jet axis switches, x_{as}/h_o, also increases. The relationship between the jet axis-switch height and orifice AR is presented in Fig. 11. The height of the first jet axis switch ($x_{as,1}$) is marked with a downward pointing triangle, the second jet axis switch ($x_{as,2}$) with a rightward pointing triangle, and the third jet axis switch ($x_{as,3}$) with an upward pointing triangle. The jet axis-switch height calculated based on the velocity width is plotted with gray triangles while the axis-switch height based on the vortex trajectories is plotted with black triangles. Finally, the heights where the vortex ring completes the first axis switch, $x_{T/2}$, are plotted as open blue diamonds, while the heights where the vortex ring completes the second axis switch (i.e., a full period of the axis-switching oscillation), x_T, are marked by open blue circles.

Based on the data plotted in Fig. 11, the jet axis-switch heights increase linearly with AR_o. A linear relationship between AR_o and axis-switch height (or AR_o and axis-switch period) has also been shown in prior studies of isolated vortex rings [25] and of vortex rings in jets [18,26]. The jet axis-switch height based on velocity is generally in good agreement with the axis-switch height based on the vortex trajectories for the first two switches, although the results from the latter follow a linear trend more precisely than the former. The third axis-switch height based on the jet velocity width is not plotted in Fig. 11 because tangency in the jet width curves and multiple crossover points introduced some ambiguity to the calculation. A best estimate of the crossover point based on jet velocity width yielded an axis-switch height 10%–40% further downstream than the axis-switch height based on the vortex paths. This implies that above a height of $x_{as,2}$ the relative influence of momentum diffusion on the jet's shape, as compared to axis-switching, has become more significant. The last axis-switching milestones detected in the $AR_o = 4$ ($x_{as,3}$) and $AR_o = 6$ (x_T) jets occur further downstream than expected, thereby deviating from the frequency of axis switching observed when the vortex rings were lower in the jet. At this point in the flow the vortex rings are very weak so self-induced deformations have slowed considerably, as has advection due to self-induction. It is conceivable that the vortex rings here are carried along by

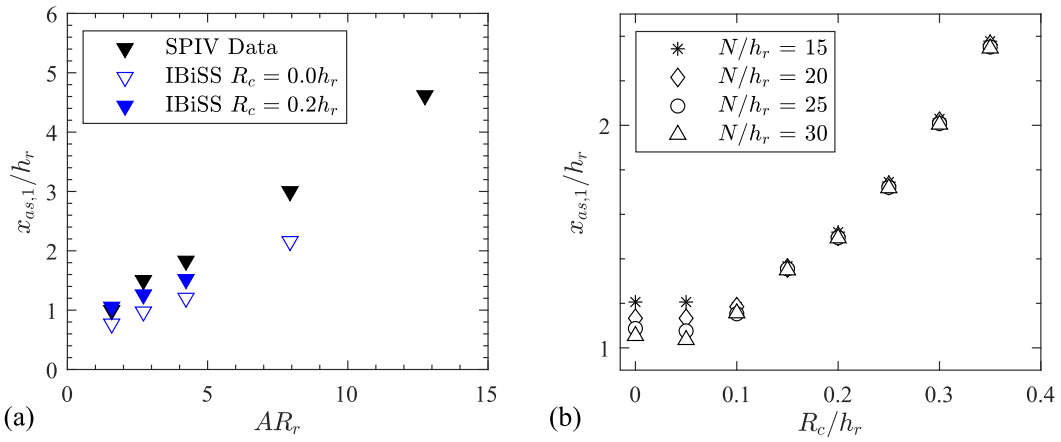

FIG. 12. Model results for (a) variation of the vortex ring axis-switching height with AR_r from SPIV data (black symbols) and IBiSS simulations (blue symbols) and (b) influence of Rankine vortex core size and vortex axis line segment density on IBiSS axis-switching height prediction for $AR_r = 4.2$.

the increasingly dominant steady component of the velocity field which characterizes the far field of a developed synthetic jet [3,7]. Thus the final axis-switching oscillations of the vortex rings would be stretched out more in the streamwise direction than they were lower in the jet, where the rings were propelled by self-induction. Finally, at $AR_o = 13$ and 19 the vortex rings bifurcated before they could complete their first axis switch. Therefore, only $x_{as,1}$ could be calculated for those cases.

To compare the experimental axis-switch data to IBiSS simulations the data had to be replotted based on the vortex ring width h_r and vortex ring aspect ratio AR_r because IBiSS does not model the actuator orifice. The height of the first axis switch based on the vortex trajectories from the experimental data (black symbols) and IBiSS (blue symbols) is plotted in Fig. 12(a). IBiSS results at the highest AR_r tested are not available because the simulations diverged due to the solver's inability to handle the very close approach and/or collisions of the antiparallel vortices in those cases. The results from the base solver, which employs an irrotational vortex model, are plotted as open blue symbols. The slope of the IBiSS results matches the SPIV data fairly well; however, there is an offset in the level between the experiment and the model. Specifically, IBiSS predicts the axis-switch height to be closer to the orifice than indicated by the experimental data.

Some of this discrepancy between the SPIV data and IBiSS results relates to the irrotational vortex model. Vortices with an infinitesimally thin vortex core experience higher local self-induction than vortices with finite-width cores, which causes the vortex ring to deform more rapidly. To study this effect, a version of IBiSS was developed which replaces the standard irrotational vortex profile in the Biot-Savart relation with a finite-width Rankine profile.

The physical vortex core radii captured in instantaneous frames and ensemble-averaged phase-locked SPIV data sets were estimated in a two-step process. First, the circulation about concentric circles of growing radii centered on the vortex axis was obtained by integration. The integration circuits were automatically deformed where necessary to prevent encircling the adjacent counterrotating vortex. Next the radial circulation distribution was fit with a Lamb-Oseen vortex profile. That fitting process yielded the vortex core radius of an equivalent axisymmetric Lamb-Oseen vortex. As an example, at a height of $x/h_r \approx 1$ in the $AR_o = 6$ jet, the calculated vortex core radius was between $R_c/h_r = 0.40$ and 0.51. Note that the vortex core is distorted into a noncircular shape in the minor axis plane due to the proximity of its counterrotating partner in the dipole. Therefore, the average vortex core radius can exceed $R_c/h_r = 0.5$ without the physical vortices overlapping, as is implied by $R_c/h_r > 0.5$. Modeling the vortex ring core geometry estimated from the SPIV data was not possible because IBiSS simulations became numerically unstable at core radii of

$R_c/h_r \geqslant 0.25$–0.35, depending on the AR_r. Instead, a reliably stable value of $R_c/h_r = 0.2$ was simulated in IBiSS to investigate the effect of employing a finite-width core. The results are plotted with blue closed symbols in Fig. 12(a). As expected, the solver with the more realistic vortex core model predicts that the vortex rings will complete an axis switch farther downstream than the solver with the irrotational vortex model does.

The effect of vortex core radius on the vortex ring deformations is explored in more detail in Fig. 12(b). IBiSS was run with the Rankine vortex model for core radii between $R_c/h_r = 0$ and 0.35. The number of line segments in the vortex ring was also varied between densities of $N/h_r = 15$ and 30 with these cases differentiated in Fig. 12(b) by different symbol types. In this study, only a single AR was tested, $\mathrm{AR}_r = 4.2$, which corresponds to the $\mathrm{AR}_o = 6$ case. As expected, increasing the core radius also increased the axis-switch height due to the reduction in local self-induction. This effect became stronger with increasing R_c. At small core sizes the axis-switch height also depended on the number of line segments used to model the ring. As the line segment density was increased the axis-switch height dropped because a more finely resolved curve has higher local curvature and therefore higher self-induction. As the core radius was increased, however, the predicted axis-switch height became less sensitive to N/h_r, presumably because a larger core radius diminishes the significance of the closest line segments.

The particular vortex profile and number of line segments used in the model are not the only factors influencing the axis-switch height. Extracting an axis-switch height from IBiSS also assumes that the vortex ring forms immediately at the orifice, i.e., at $x/h_r = 0$, which obviously does not occur in the physical synthetic jet. Furthermore, IBiSS does not account for the momentum of the fluid slug ejected by the actuator which likely contributed to the initial downstream translation of the vortex ring. Therefore, IBiSS is not a tool for quantitative predictions but instead a means to gain insight into the qualitative behavior and inviscid dynamics of vortex rings.

D. Effect of vortex dynamics on jet centerline velocity

The time-averaged centerline velocity of the jet for all five AR orifices is presented in Fig. 13. The centerline velocity is plotted on the vertical axis normalized by the maximum centerline velocity of that jet. The axial distance from the orifice along the centerline is plotted on the horizontal axis and is normalized by $x_{as,1}$ so that, at a given horizontal position, the vortex rings are at a similar point in their axis-switching cycle for all of the cases. The $\mathrm{AR}_o = 2$ results are presented at the bottom of the plot and each subsequent case is offset upward 0.5 vertical units. The centerline velocity corresponding to the AR_o label on the right is plotted as a black solid line, while the $\mathrm{AR}_o = 6$ results are plotted in the background for all cases as a gray dashed line for comparison. In all cases, the centerline velocity near the orifice dips down to zero at $x/x_{as,1} = 0$, as is expected for a zero-net-mass-flux jet. Moving up from the orifice, the effect of the suction cycle dissipates and the vortex ring circulation strength grows, which causes the centerline velocity to rise. Further downstream, the centerline velocity profile develops two peaks: The first sits within $0 < x/x_{as,1} < 1$ and the second is found within $1 < x/x_{as,1} < 2$. These local peaks in the centerline velocity are subtle at the lower AR but become more pronounced as AR increases. The attenuated first velocity peak in the $\mathrm{AR}_o = 2$ case may relate to a more axisymmetric behavior in this jet as compared with the higher AR cases.

Similar double-peak centerline velocity distributions have been measured in other rectangular orifice synthetic jet experiments and were attributed to secondary structures within the jet [2,28]. IBiSS was used to explore the dynamics involved with these peaks. Instead of using constant circulation strength for the vortex ring, the profile of circulation growth and decay with time, which was extracted from the time-averaged SPIV data, was used. Simulations were run for the various AR cases. Interestingly, IBiSS was able to predict the presence of these centerline velocity peaks despite being an inviscid solver which does not model the secondary structures.

An example circulation profile extracted from the SPIV data in the major axis plane of the $\mathrm{AR}_o = 13$ jet is shown in Fig. 14(a). Circulation was computed by integrating the velocity field around polygons, which were manually drawn to encompass the full vortex while excluding adjacent

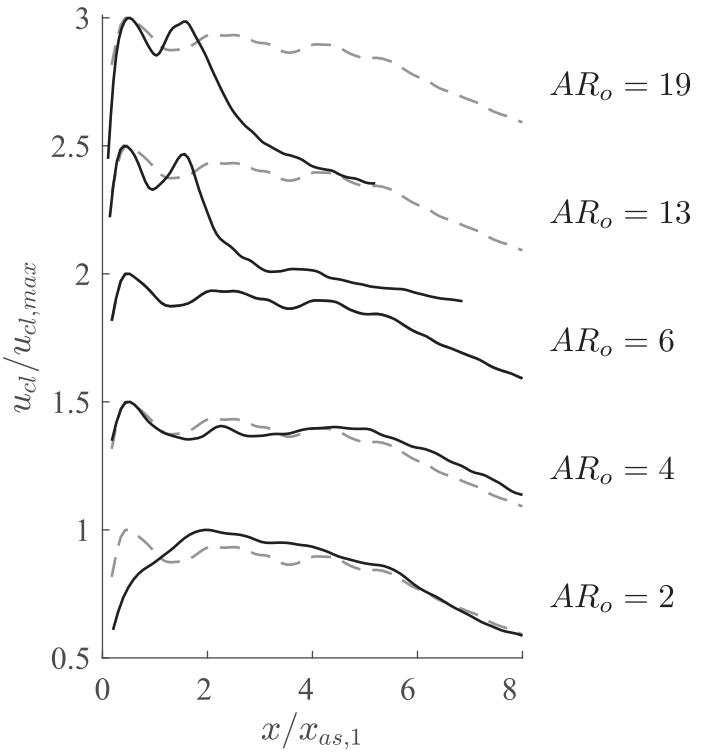

FIG. 13. Axial variation in mean jet centerline axial velocity with each AR_o case offset up 0.5 vertical units (black solid line) and overlaid on the $AR_o = 6$ case (gray dashed line) for comparison.

vortices and secondary structures. The circulation values computed from the phase-locked data are plotted with gray diamonds, while the spline fit to these data, which was used to set the dynamic circulation strength in IBiSS, is represented by a black solid line. The circulation profile of the $AR_o = 13$ vortex ring has four distinct regions starting with an initial rapid strengthening of the ring

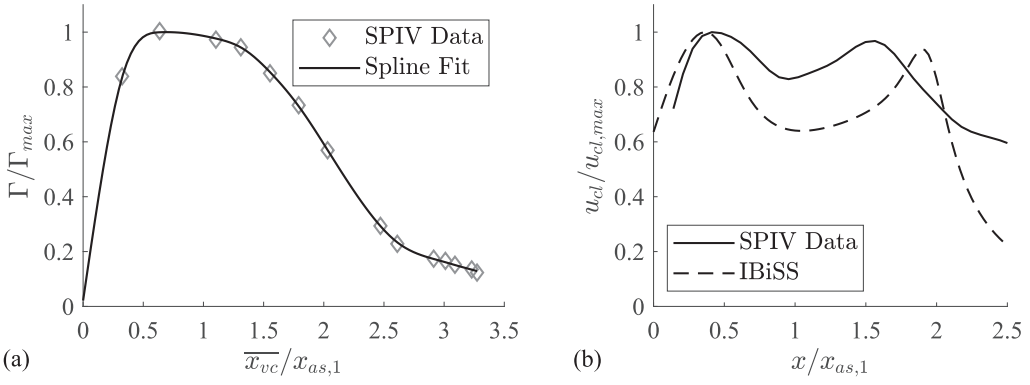

FIG. 14. The $AR_o = 13$ axial variation in (a) vortex ring circulation from phase-locked SPIV data (diamonds) with a spline fit (solid line) and (b) mean jet centerline axial velocity from SPIV data (solid line) and IBiSS simulation (dashed line).

as the vortex forms. After achieving a maximum circulation around $\overline{x_{vc}}/x_{as,1} = 0.6$ the circulation then declines gradually during the short pseudoinviscid advection phase. However, once the vortex ring reaches an average height of $\overline{x_{vc}}/x_{as,1} \approx 1.5$ the leading ends of the ring in the major axis plane collide with each other and circulation drops rapidly due to vorticity annihilation and reconnection. In the final region of the profile above $\overline{x_{vc}}/x_{as,1} \approx 2.7$ the decline in circulation drops in rate again as the colliding vortices diverge and vorticity reconnection slows or ceases. These regions of the circulation profile along with the associated dynamics are discussed in more detail in Ref. [29].

Figure 14(b) compares the centerline velocity profile from the IBiSS results (dashed line) to the SPIV data (solid line) for the $\mathrm{AR}_o = 13$ case. IBiSS was run with an AR_r of 6.1 until the point where the vortex ring achieved an average height of $2.1x_{as,1}$. The measured vortex ring AR, i.e., $\mathrm{AR}_r = 7.9$, was not used because the simulation had to be stopped too early to prevent solution divergence when the ring approached a collision in the major axis plane. Both the measured and simulated profiles exhibit two peaks in centerline velocity. Some of the differences between the IBiSS and the SPIV results can be related to aspects of the synthetic jet not modeled by the solver. For example, the centerline velocity at the orifice ($x/x_{as,1} = 0$) does not trend to zero in the IBiSS simulation because the suction phase of the actuator is not modeled. Also, the first peak in both velocity profiles occurs at a similar height; however, without the effect of the suction cycle, the IBiSS peak is shifted slightly closer to the orifice.

The first peak appears in the time-averaged centerline velocity profile for a couple of reasons. One is that the effect of suction dissipates with distance from the orifice. The other relates to the formation of the vortex. By the Biot-Savart law, induced velocity decreases with the square of distance from the vortex. Therefore, everything else being equal, the induced centerline velocity is highest when the vortex ring is narrowest in either the major or minor axis plane. Although the minor axis of the vortex ring is narrowest in the incipient ring, before axis-switching deformations begin, the circulation strength is low at that time. Therefore, the peak centerline velocity occurs at a height which is an optimal balance between rising circulation strength, increasing vortex separation distance, and changing duration of the vortex proximity to a particular point.

As the vortex ring deforms, the vortices in the minor axis plane spread apart from each other, which tends to reduce the velocity induced on the jet centerline by the minor axis portion of the vortex ring. Concurrently, in the major axis plane the vortex ring converges towards centerline, but from much farther away. Due to the dependence of induced velocity on the square of distance, the net effect is a reduction in centerline velocity. Note that the trough in centerline velocity occurs in both profiles at the height of the first axis switch ($x/x_{as,1} = 1$), which is by definition the point where the vortices in the major and minor axis planes are an equal distance from the centerline [Fig. 14(b)].

Downstream of $x_{as,1}$ the vortices in the major axis plane continue to converge, causing centerline velocity induction to rise. In IBiSS, the second peak in the centerline velocity coincides with the height where the vortices in the major axis plane achieve minimum separation from the jet centerline which is $x_{\Delta z,\min}/x_{as,1} = 1.90$ [Fig. 14(b)]. Although the height of minimum vortex separation is essentially the same in the SPIV measurement (i.e., $x_{\Delta z,\min}/x_{as,1} = 1.96$), the velocity peak in the experimental data occurs well upstream of this point and has a lower prominence than in IBiSS. The shift and attenuation of the centerline velocity peak are due to the bifurcation of the vortex ring. Before the vortex ring completes its first axis switch, the outer regions of the vortices in the major axis plane collide and vorticity reconnection starts. As the circulation strength of that portion of the ring declines so does the magnitude of induced velocity. Furthermore, the reconnected vorticity accumulates in bridge vortices whose rotational directions induce a downward velocity on the centerline, opposite the direction of induction from the rest of the vortex ring [29,46]. Together these changes in the distribution of circulation explain both the rapid drop in centerline velocity in the SPIV data and the fact that the second peak is attenuated and occurs closer to the orifice than in the IBiSS results. The influence of the bridge vortices is not captured by IBiSS because the solver does not model viscous processes like vorticity reconnection. In fact, the vortex dynamics predicted

by IBiSS when the vortex ring reaches $x \geqslant x_{T/2}$ is inaccurate; therefore, the solver was not run past this point.

The effect of vortex ring bifurcation on the jet persists for a long distance downstream. In the $AR_o = 2$, 4, and 6 jets the centerline velocity remains relatively high out to $x/x_{as,1} = 5$, after which all three decline at a similar rate (Fig. 13). In contrast, the centerline velocity of the $AR_o = 13$ and 19 jets declines rapidly around $x/x_{as,1} \approx 1.6$ due to the vortex ring bifurcation and remains low up to the edge of the measurement domain. Although not apparent from Fig. 13, the reduction in the jet momentum along the centerline is accompanied by an increase in momentum off centerline along paths aligned with the two smaller vortex rings produced by the bifurcation [29].

The prominence of the centerline velocity peaks and the depth of the troughs in the SPIV data increases with the orifice AR [Fig. 14(b)]. A similar trend was observed in IBiSS simulations. The change in the peak prominence relates to the magnitude of the variation in Δy_{vc} and Δz_{vc} with axial vortex position. In low AR vortex rings axis-switching deformations only produce small changes in Δy_{vc} and Δz_{vc}; therefore, the distance from the vortex to the centerline varies little with time. As AR is increased the deformations become more extreme, and the distance between the vortex and the jet centerline ranges from very close at the height of the axis-switch completion to distant at the jet width crossover heights. Therefore, the prominence of the centerline velocity peaks is also strongly correlated with the inviscid dynamics of the vortex ring.

V. CONCLUSION

The behavior and performance of synthetic jets are closely tied to the dynamics of vortex rings, which are a dominant feature of the early jet. When a synthetic jet actuator employs a nonaxisymmetric orifice or nozzle the self-induced deformations of the vortex rings are responsible for changes in the shape of the jet as well as the distribution of momentum in the jet and the entrainment rate.

In this study, rectangular orifice synthetic jets issuing into quiescent fluid were investigated experimentally using SPIV and modeling via an inviscid Biot-Savart solver. To explore the effect of orifice shape on the vortex dynamics in the jet, orifice AR values of 2, 4, 6, 13, and 19 were tested. The self-induced deformations of the vortex rings in the synthetic jet gave rise to periodic axis switching of the ring in a manner similar to what has been reported in isolated noncircular vortex rings. The axis-switch height of the jet based on the crossover point where the jet width in one symmetry plane exceeded the width in the other was calculated using two methods. In the first method the width of the jet was determined from the half-velocity points in the cross-stream velocity profiles, while the second method defined the width using the vortex trajectories. These two methods yielded similar results for the first few axis switches of the jet, which indicates that the vortex ring oscillations were the primary driver of the jet shape and momentum distribution in the near field. Above the second axis-switch point, however, the velocity width of the jet changed more slowly than the width of the vortex rings. This suggests that this is the start of the transition zone from the vortex dominated near field to the far field, where diffusion of momentum is the dominant factor influencing the jet's shape. The height at which the jet switched axes increased linearly with the orifice AR, and the jets with the lowest orifice AR values tested axis switched two or three times before the vortices lost coherence. However, the jets with an orifice AR greater than 6 only axis switched once and the analysis of the vortex rings revealed that they never fully completed the axis-switching cycle to return to a roughly planar configuration. The PIV results from prior studies of moderate to high AR synthetic jets have also indicated that only a single axis switch occurred; however, the reason axis switching ceased was not explored. The present study revealed that the cessation of axis switching was due to bifurcation of the vortex rings when their AR were sufficiently high. Furthermore, based on the estimated AR of the vortex rings produced by the different synthetic jet actuator orifices, the critical threshold for vortex ring bifurcation in synthetic jets appears to be consistent with the limit established in isolated vortex rings, i.e., $AR_r = 4$–5. A comparison of the axial variation in the mean jet centerline velocity for the different jets revealed a double peak in

the profile which became more pronounced with increasing orifice AR. Similar double peaks in the centerline velocity of synthetic jets have been observed in other studies, although a detailed explanation for their origin was not offered by those authors. By analyzing the complementary experimental data and simulation results, the present study revealed that these peaks are most likely due to the inviscid dynamics of the deforming vortex rings and not secondary structures as previously hypothesized. In general, the shape and momentum of the synthetic jets was strongly influenced by the dynamics of the primary vortex rings and those dynamics changed appreciably with the aspect ratio of the actuator orifice.

ACKNOWLEDGMENT

This material is based upon work supported by the National Science Foundation Graduate Research Fellowship Program under Grant No. DGE 1144083.

[1] F. Hussain and H. S. Husain, Elliptic jets. Part 1. Characteristics of unexcited and excited jets, J. Fluid Mech. **208**, 257 (1989).
[2] T. Van Buren and M. Amitay, Comparison between finite-span steady and synthetic jets issued into a quiescent fluid, Exp. Therm. Fluid Sci. **75**, 16 (2016).
[3] B. L. Smith and A. Glezer, The formation and evolution of synthetic jets, Phys. Fluids **10**, 2281 (1998).
[4] B. L. Smith and G. W. Swift, A comparison between synthetic jets and continuous jets, Exp. Fluids **34**, 467 (2003).
[5] X. Xia and K. Mohseni, Transitional region of a round synthetic jet, Phys. Rev. Fluids **3**, 011901(R) (2018).
[6] R. Holman, Y. Utturkar, R. Mittal, B. L. Smith, and L. Cattafesta, Formation criterion for synthetic jets, AIAA J. **43**, 2110 (2005).
[7] X. Xia and K. Mohseni, Far-field momentum flux of high-frequency axisymmetric synthetic jets, Phys. Fluids **27**, 115101 (2015).
[8] A. Glezer, M. Amitay, and A. M. Honohan, Aspects of low- and high-frequency actuation for aerodynamic flow control, AIAA J. **43**, 1501 (2005).
[9] M. Amitay, D. Pitt, and A. Glezer, Separation control in duct flows, J. Aircr. **39**, 616 (2002).
[10] J. A. N. Farnsworth, J. C. Vaccaro, and M. Amitay, Active flow control at low angles of attack: Stingray unmanned aerial vehicle, AIAA J. **46**, 2530 (2008).
[11] M. Chaudhari, B. Puranik, and A. Agrawal, Heat transfer characteristics of synthetic jet impingement cooling, Int. J. Heat Mass Transf. **53**, 1057 (2010).
[12] D. Guo, A. W. Cary, and R. K. Agarwal, Numerical simulation of vectoring of a primary jet with a synthetic jet, AIAA J. **41**, 2364 (2003).
[13] H. Wang and S. Menon, Fuel-air mixing enhancement by synthetic microjets, AIAA J. **39**, 2308 (2001).
[14] B. L. Smith and A. Glezer, Jet vectoring using synthetic jets, J. Fluid Mech. **458**, 1 (2002).
[15] G. Godard and M. Stanislas, Control of a decelerating boundary layer. Part 1: Optimization of passive vortex generators, Aerosp. Sci. Technol. **10**, 181 (2006).
[16] E. J. Gutmark and F. F. Grinstein, Flow control with noncircular jets, Annu. Rev. Fluid Mech. **31**, 239 (1999).
[17] C.-M. Ho and E. Gutmark, Vortex induction and mass entrainment in a small-aspect-ratio elliptic jet, J. Fluid Mech. **179**, 383 (1987).
[18] L. Wang, L.-H. Feng, J.-J. Wang, and T. Li, Evolution of low-aspect-ratio rectangular synthetic jets in a quiescent environment, Exp. Fluids **59**, 1 (2018).
[19] R. J. Arms and F. R. Hama, Localized-induction concept on a curved vortex and motion of an elliptic vortex ring, Phys. Fluids **8**, 553 (1965).
[20] H. Viets and P. M. Sforza, Dynamics of bilaterally symmetric vortex rings, Phys. Fluids **15**, 230 (1972).

[21] M. R. Dhanak and B. D. Bernardinis, The evolution of an elliptic vortex ring, J. Fluid Mech. **109**, 189 (1981).
[22] Y. Oshima, N. Izutsu, K. Oshima, and A. K. M. F. Hussain, Bifurcation of an elliptic vortex ring, Fluid Dyn. Res. **3**, 133 (1988).
[23] M. Cheng, J. Lou, and T. T. Lim, Evolution of an elliptic vortex ring in a viscous fluid, Phys. Fluids **28**, 037104 (2016).
[24] T. Kambe and T. Takao, Motion of distorted vortex rings, J. Phys. Soc. Jpn. **31**, 591 (1971).
[25] M. Kiya and H. Ishii, Deformation and splitting of Pseudo-elliptical vortex rings, in *Advances in Turbulence 3*, edited by A. V. Johansson and P. H. Alfredsson (Springer, Berlin, Heidelberg, 1991), pp. 52–60.
[26] F. F. Grinstein, Self-induced vortex ring dynamics in subsonic rectangular jets, Phys. Fluids **7**, 2519 (1995).
[27] M. Amitay and F. Cannelle, Evolution of finite span synthetic jets, Phys. Fluids **18**, 054101 (2006).
[28] T. Van Buren, E. Whalen, and M. Amitay, Vortex formation of a finite-span synthetic jet: Effect of rectangular orifice geometry, J. Fluid Mech. **745**, 180 (2014).
[29] J. C. Straccia and J. A. N. Farnsworth, Vortex ring bifurcation and secondary structures in a finite-span synthetic jet, J. Fluid Mech. **903**, A42 (2020).
[30] A. Lindstrom and M. Amitay, Effect of orifice geometry on synthetic jet evolution, AIAA J. **57**, 2783 (2019).
[31] L. Wang and L.-H. Feng, The interactions of rectangular synthetic jets with a laminar cross-flow, J. Fluid Mech. **899**, A32 (2020).
[32] M. Jabbal and S. Zhong, Particle image velocimetry measurements of the interaction of synthetic jets with a zero-pressure gradient laminar boundary layer, Phys. Fluids **22**, 063603 (2010).
[33] T. Berk and B. Ganapathisubramani, Effects of vortex-induced velocity on the development of a synthetic jet issuing into a turbulent boundary layer, J. Fluid Mech. **870**, 651 (2019).
[34] M. Gharib, E. Rambod, and K. Shariff, A universal time scale for vortex ring formation, J. Fluid Mech. **360**, 121 (1998).
[35] C. O'Farrell and J. O. Dabiri, Pinch-off of non-axisymmetric vortex rings, J. Fluid Mech. **740**, 61 (2014).
[36] D. Adhikari, Some experimental studies on vortex ring formation and interaction, Master's thesis, National University of Singapore, 2009.
[37] B. Wieneke, PIV uncertainty quantification from correlation statistics, Meas. Sci. Technol. **26**, 074002 (2015).
[38] J. C. R. Hunt, A. A. Wray, and P. Moin, *Center for Turbulence Research Proceedings of the Summer Program 1988* (Stanford University, Stanford, 1988), pp. 193–208.
[39] J. Jeong and F. Hussain, On the identification of a vortex, J. Fluid Mech. **285**, 69 (1995).
[40] M. Kiya, K. Toyoda, H. Ishii, M. Kitamura, and T. Ohe, Numerical simulation and flow-visualization experiment on deformation of pseudo-elliptic vortex rings, Fluid Dyn. Res. **10**, 117 (1992).
[41] F. R. Hama, Progressive deformation of a curved vortex filament by its own induction, Phys. Fluids **5**, 1156 (1962).
[42] N. Didden, On the formation of vortex rings: Rolling-up and production of circulation, Z. Angew. Math. Phys. **30**, 101 (1979).
[43] T. Maxworthy, Some experimental studies of vortex rings, J. Fluid Mech. **81**, 465 (1977).
[44] J. M. Shuster and D. R. Smith, Experimental study of the formation and scaling of a round synthetic jet, Phys. Fluids **19**, 045109 (2007).
[45] S. Kida, M. Takaoka, and F. Hussain, Collision of two vortex rings, J. Fluid Mech. **230**, 583 (1991).
[46] M. V. Melander and F. Hussain, Center for Turbulence Research Proceedings of the Summer Program 1988 (Ref. [38]), pp. 257–286.